Phase drift on networks of coupled crystal oscillators for precision timing

Pietro-Luciano Buono, Visarath In, Patrick Longhini, Loni Olender, Antonio Palacios, and Steven Reeves

Phys. Rev. E **98**, 012203 — Published 5 July 2018

DOI: 10.1103/PhysRevE.98.012203

Phase Drift on Networks of Coupled Crystal Oscillators For Precision Timing

Pietro-Luciano Buono,* Visarath In, Patrick Longhini,† Loni Olender, Antonio Palacios,‡ and Steven Reeves§
*Faculty of Science, University of Ontario Institute of Technology,
2000 Simcoe St N, Oshawa, ON L1H 7K4, CANADA
†Space and Naval Warfare Systems Center Pacific, Code 71730,
53560 Hull Street, San Diego, CA 92152-5001, USA.
‡ Nonlinear Dynamical Systems Group, Department of Mathematics,
San Diego State University, San Diego, CA 92182, USA.
§Department of Applied Mathematics and Statistics,
University of California Santa Cruz, Santa Cruz, CA 95064, USA
(Dated: June 22, 2018)

Precise time dissemination and synchronization have been some of the most important technological tasks for several centuries. No later than Harrison's time, it was realized that precise time-keeping devices having the same stable frequency and precisely synchronized can have important applications in navigation. In modern times, satellite-based global positioning and navigation systems such as the GPS use the same principle. However, even the most sophisticated satellite navigation equipment cannot operate in every environment. In response to this need, we present a computational and analytical study of a network-based model of a high-precision, inexpensive, Coupled Crystal Oscillator System and Timing (CCOST) device. A bifurcation analysis (carried out by the authors in a related publication) of the network dynamics shows a wide variety of collective patterns, mainly various forms of discrete rotating waves and synchronization patterns. Results from computer simulations seem to indicate that, among all patterns, the *standard* traveling wave pattern in which consecutive crystals oscillate out of phase by $2\pi/N$, where N is the network size, leads to phase drift error that decreases as $1/N$ as opposed to $1/\sqrt{N}$ for an uncoupled ensemble. The results should provide guidelines for future experiments, design and fabrication tasks.

PACS numbers: 74.81.Fa, 85.25.Dq, 43.25.-x, 85.25.-j

I. INTRODUCTION

Precise time is crucial to a variety of economic activities around the world. Communication systems, electrical power grids, and financial networks all rely on precision timing for synchronization and operational efficiency. The free availability of GPS[1] time has enabled cost savings for industrial and scientific developments that depend on precise time and has led to significant advances in capability. For example, wireless telephone and data networks use GPS time to keep all of their base stations in synchronization. This allows mobile handsets to share limited radio spectrum more efficiently. Similarly, digital broadcast radio services use GPS time to ensure that the signals from all radio stations arrive at receivers in lockstep, so that listeners can tune between stations with minimum delay.

However, even the most sophisticated satellite navigation equipment cannot operate in every environment. And even under perfect weather and environmental conditions, mechanical failure can still occur and hinder accessibility. In fact, many of the 32 satellites in the GPS constellation are operating past their intended lifespan or suffering from equipment failure. There have been a few launch incidents in past years, and the Air Force, which maintains the 30-year-old network, is overburdened with competing space priorities. Thus it is reasonable to wonder what would happen if the U.S. Global Positioning System is not available due to environmental or to complete mechanical failure.

In response to this need, we investigate in this manuscript the timing error response of a coupled crystal oscillator system (CCOST) device as a proposed solution. The fundamental idea is to exploit the collective response of a coupled network system to significantly reduce phase drift or phase error. Thus, in previous work[2], we studied in great detail the various patterns of oscillations that can emerge in network topologies in the form of unidirectionally and bidirectionally coupled rings of crystals oscillators. In a nutshell, the study led to the classification of two classes of patterns. One class includes a variety of discrete rotating waves which emerge via the equivalent of symmetry-breaking Hopf bifurcations from a trivial equilibrium. Another class includes symmetry-preserving bifurcations that yield synchronization states. Then a natural issue to investigate is which pattern, among all possible choices, can yield the smallest *timing error* or *phase error*. It should be noted that in this paper we use the terms "timing error" and "phase error" interchangeably. Regardless of the terminology, phase error refers to the changes or variations in the phase of an oscillator over a long period of time. In simpler words, it shows how much time is lost every second. Possible sources of phase drift include environmental fluctuations, noise, and imperfections of materials. Thus, performance or robustness of a precision timing device is evaluated by examining its phase error response through computer simulations that incorporate the effects of noise in the corresponding mathematical models. In this manuscript we use the results of the corresponding bifurcation analy-

sis to investigate how the phase error scales as function of the number of nodes in the network and of the strength of the coupling parameter.

The *standard* practice in precision timing is to average out the timing of multiple (uncoupled) clocks. For instance, at the United States Naval Observatory time is measured by averaging the time of an ensemble of (uncoupled) atomic clocks. In this case, phase error scales as $1/\sqrt{N}$. In this manuscript, we seek to show proof of concept that an ensemble of coupled crystal oscillators can produce a phase error that scales, at least, as $1/N$. Crystal oscillators were chosen because they are readily available, inexpensive and require low power for operation. However, the fundamental idea of performance enhancement via collective behavior is a model-independent feature which should apply to any network of coupled nonlinear oscillators, provided that the collective oscillations are, qualitatively, the same.

This paper is organized as follows. First, some historical information and background information on precision timing and crystal oscillators, including circuit diagrams and model equations for one single CCOST system, are presented in Sections II and III. The network topologies with governing equations, along with a description of the patterns of oscillation from[2] are found in Section IV. In Section V the model equations are recast to include a stochastic component in order to model environmental fluctuations and noise in electronic circuits. The stochastic process allows us to define and study phase error, our tool for measuring the timing performance.

This section on phase error is presented as an experiment in simulation. First an uncoupled ensemble is studied to serve a control group for comparison. Then two coupled networks are examined, these networks are unidirectionally and bidirectionally coupled. The next section presents some preliminary results from experiments from SPAWAR Systems Center Pacific. This paper concludes with a discussion on the presented results and future works.

II. HISTORY OF PRECISION TIMING

Historically, the inability to determine longitude accurately made navigation on the open seas difficult and treacherous. In the Renaissance era, when Europe began its exploration, determining longitude required comparing the time at the current location with the time at a known location, say the Greenwich meridian. However, no shipboard clocks could determine time to an accuracy sufficient for navigational purposes. Heads of several seafaring nations offered great prizes for a solution to the problem of longitude. In the early 18th century, the Longitude Prize offered by Britain led to the development of the ship's chronometer. [3] This device was so amazingly workable that it remained in use unchanged in its essential elements until the electronic era of the early 20th century. Following World War I and the development of the electronic oscillator and radio communications, the U.S. Navy took an ever more active role in the development of emerging Precision Time and Time Interval (PTTI) technologies. The U.S. Naval Observatory (USNO), the Naval Research Laboratory (NRL) and, after World War II, the Office of Naval Research (ONR), the Defense Advanced Research Projects Agency (DARPA) and the National Science Foundation[4] were important players in the development of the technology that makes up the current *state of the art* in PTTI[5].

The advances that had been made in high-frequency electronics during the second World War, specifically radar research, set the stage for the development of atomic clocks. In 1942 the Joint Chiefs of Staff established a Radio Propagation Laboratory at the National Bureau of Standards (NBS), now the National Institute of Standards and Technology (NIST). The Radio Propagation Laboratory developed the world's first atomic clock in 1948. This clock was based on the measurement of a spectroscopic absorption line of ammonia. Because the stability of this design was no better than their high-quality quartz oscillators, the ammonia system was quickly abandoned for the greater potential accuracy of the cesium atomic beam device. The heart of the cesium device was a microwave cavity developed in 1948 by Norman Ramsey of Harvard University (Ramsey received the Nobel Prize for this work in 1989.)

Immediately following the launch of the first artificial Earth-orbiting satellite, Sputnik, by the Soviet Union in 1957, the Navy set up the Naval Space Surveillance System (NAVSPASUR). In 1964, Roger Easton of the NRL put forward a concept for an improved navigation system that would orbit precision clocks. Signals from such a satellite could provide more precise navigation as well as precise time signals that were available worldwide. To achieve this goal, NRL started programs to develop improved quartz frequency standards suitable for spaceflight. Soon thereafter, the Timation program, which involved atomic clocks in space, was established. These space-qualified atomic clocks were then used in the Global Positioning System (GPS), GPS became a joint service program in 1973, with the Air Force designated executive agent for the system.

Since 1976 the length of a second has been defined as the frequency of a specific resonant mode of the cesium atom. The frequency inaccuracy of the cesium clocks is approximately $8.64ns/day$. In comparison the typical watch crystal has an error of about 20ppm, which is about $1.73s/day$. The increased accuracy and precision comes with a price. Typical cost range of crystal oscillators are in the few dollars while a cesium clock can be in the order of $40,000. Currently, the accuracy of the NIST atomic clock, called NIST-F2[6], is on the order of $1\text{x}10^{-16}$, making it on the order of three times as accurate as its predecessor NIST-F1, which had served as the standard since 1999. Both clocks use a 'fountain' of cesium atoms to determine a precise measure of a second. The key operational difference is that F1 oper-

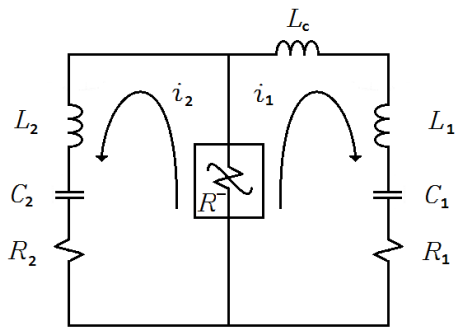

FIG. 1: Two-mode crystal oscillator circuit. A second set of spurious RLC components (R_2, L_2, C_2) are introduced by parasitic elements.[9][10]

ates near room temperature whereas the atoms in F2 are shielded within a much colder environment[7] and, thus, less portable. Lack of portability makes the case for a CCOST device even stronger.

III. MODELING

When a crystal of quartz is properly cut and mounted, it can be made to distort in an electric field by applying a voltage to an electrode near or on the crystal. This property is known as electrostriction or inverse piezoelectricity. When the field is removed, the quartz generates an electric field as it returns to its previous shape, and this can generate a voltage. The result is that a quartz crystal behaves like a circuit composed of an inductor, capacitor and resistor, with a precise resonant frequency[8], see Fig. 1.

A crystal oscillator circuit sustains oscillations by applying a voltage signal from the quartz resonator, amplifying it, and feeding it back to the resonator. The rate of expansion and contraction of the quartz is the resonant frequency, and is determined by the cut and size of the crystal. When the energy of the generated output frequencies matches the losses in the circuit, an oscillation can be sustained. The frequency of the crystal can be slightly adjusted by modifying the attached capacitances. A varactor, a diode with capacitance depending on applied voltage, is often used in voltage-controlled crystal oscillators, VCOs. The analog port of the VCO chip is modeled by a nonlinear resistor R^-, see Fig. 1, that obeys the voltage-current relationship[11]

$$v = -ai + bi^3,$$

where a and b are constant parameters. This analog port of the VCO is the expression of the crystal as an electronic oscillator. A major reason for the wide use of crystal oscillators is their high Q factor. This is a dimensionless parameter that indicates how underdamped an oscillator is. For a crystal oscillator, it can be defined as the ratio of the resonant frequency with respect to the half-power bandwidth, i.e., the bandwidth over which the power of vibration is greater than half the power at the resonant frequency. Higher Q indicates that the oscillations die out more slowly. A typical Q value for a quartz oscillator ranges from 104 to 106, compared to perhaps 102 for an LC oscillator. The maximum Q for a high stability quartz oscillator can be estimated as $Q = 1.6\,E07/f$, where f is the resonance frequency in megahertz.

A. Two-Mode Oscillator in Dimensionless Form

The inductance of the leads connecting the crystal to the VCO port is represented by L_c. In addition, parasitic elements can be represented by a series resonator (L_2, C_2, R_2) connected in parallel with the nonlinear resistor. The resulting circuit, depicted in Fig. 1, forms a two-mode resonator model. Applying Kirchhoff's voltage law yields the following governing equations

$$L_j\frac{d^2i_j}{dt^2}+R_j\frac{di_j}{dt}+\frac{1}{C_j}i_j=\left[a-3b(i_1+i_2)^2\right]\left[\frac{di_1}{dt}+\frac{di_2}{dt}\right], \tag{1}$$

where $j = 1, 2$ and L_c has been included in L_1. Laurin and Balmain[11] employed the method of averaging to study the response of the two-mode oscillator Eq. (1). Next we provide a brief review of their analysis. The aim is not to duplicate their work but rather to introduce a dimensionless version of the equations and a different notation, which facilitates a natural extension of the averaging method to the coupled network system. We start by re-scaling time as $t = \sqrt{L_1C_1}\tau$. Letting $\Omega_1^2 = 1$, $\Omega_2^2 = \frac{L_1}{L_2}\frac{C_1}{C_2}$, $L_r = \frac{L_1}{L_2}$, and $\varepsilon = \sqrt{\frac{C_1}{L_1}}$, and relabeling τ as time t, Eq. (1) becomes:

$$\begin{aligned}
&\frac{d^2i_1}{dt^2}+\Omega_1^2i_1 = \\
&\varepsilon\left\{-R_1\frac{di_1}{dt}+\left[a-3b\big(i_1+i_2\big)^2\right]\left[\frac{di_1}{dt}+\frac{di_2}{dt}\right]\right\} \\
&\frac{d^2i_2}{dt^2}+\Omega_2^2i_2 = \\
&\varepsilon L_r\left\{-R_2\frac{di_2}{dt}+\left[a-3b\big(i_1+i_2\big)^2\right]\left[\frac{di_1}{dt}+\frac{di_2}{dt}\right]\right\}.
\end{aligned} \tag{2}$$

B. Averaging

Applying the following invertible coordinates transformation to Eq. (2),

$$\begin{aligned} i_1 &= x_1\cos\phi_1; \quad i_1' = -\Omega_1 x_1\sin\phi_1; \\ i_1'' &= \Omega_1 x_1'\sin\phi_1 - \Omega_1^2 x_1\cos\phi_1 - \Omega_1 x_1\psi_1'\cos\phi_1; \\ i_2 &= x_2\cos\phi_2; \quad i_2' = -\Omega_2 x_2\sin\phi_2; \\ i_2'' &= \Omega_2 x_2'\sin\phi_2 - \Omega_2^2 x_2\cos\phi_2 - \Omega_2 x_2\psi_2'\cos\phi_2; \\ \phi_1 &= \Omega_1 t + \psi_1; \quad \phi_2 = \Omega_2 t + \psi_2, \end{aligned} \tag{3}$$

we can then re-write Eq. (2) in a more suitable form for averaging. That is,

$$\begin{bmatrix} \mathbf{x}' \\ \psi' \\ \phi' \end{bmatrix} = \begin{bmatrix} 0 \\ 0 \\ \mathbf{\Omega}^0 \end{bmatrix} + \varepsilon \begin{bmatrix} \mathbf{X}^{[1]}(\mathbf{x},\phi,\varepsilon) \\ \mathbf{\Omega}^{[1]}(\mathbf{x},\phi,\varepsilon) \\ 0 \end{bmatrix}, \tag{4}$$

where $\mathbf{x} = (x_1, x_2)$, $\phi = (\phi_1, \phi_2)$, $\psi = (\psi_1, \psi_2)$, $\mathbf{\Omega}^0 = (\Omega_1, \Omega_2)$, $\mathbf{X}^{[1]} = (X_1^{[1]}, X_2^{[1]})$ and $\mathbf{\Omega}^{[1]} = (\Omega_1^{[1]}, \Omega_2^{[1]})$. Explicitly

$$\begin{aligned} X_1^{[1]} &= \frac{1}{\Omega_1}\big\{R_1\Omega_1 x_1\sin\phi_1 + \\ &\quad \big[a - 3b\big(x_1\cos\phi_1 + x_2\cos\phi_2\big)^2\big] \\ &\quad \big[-\Omega_1 x_1\sin\phi_1 - \Omega_2 x_2\sin\phi_2\big]\big\}\sin\phi_1 \\ X_2^{[1]} &= \frac{L_r}{\Omega_2}\big\{R_2\Omega_2 x_2\sin\phi_2 + \\ &\quad \big[a - 3b\big(x_1\cos\phi_1 + x_2\cos\phi_2\big)^2\big] \\ &\quad \big[-\Omega_1 x_1\sin\phi_1 - \Omega_2 x_2\sin\phi_2\big]\big\}\sin\phi_2 \\ \Omega_1^{[1]} &= \frac{1}{\Omega_1 x_1}\big\{R_1\Omega_1 x_1\sin\phi_1 + \\ &\quad \big[a - 3b\big(x_1\cos\phi_1 + x_2\cos\phi_2\big)^2\big] \\ &\quad \big[-\Omega_1 x_1\sin\phi_1 - \Omega_2 x_2\sin\phi_2\big]\big\}\cos\phi_1 \\ \Omega_2^{[1]} &= \frac{L_r}{\Omega_2 x_2}\big\{R_2\Omega_2 x_2\sin\phi_2 + \\ &\quad \big[a - 3b\big(x_1\cos\phi_1 + x_2\cos\phi_2\big)^2\big] \\ &\quad \big[-\Omega_1 x_1\sin\phi_1 - \Omega_2 x_2\sin\phi_2\big]\big\}\cos\phi_2 \end{aligned}$$

Observe that now the first two equations in (4) are in standard form[12], so that averaging over the phase variables yield

$$\begin{bmatrix} \mathbf{x}' \\ \psi' \\ \phi' \end{bmatrix} = \begin{bmatrix} 0 \\ 0 \\ \mathbf{\Omega}^0 \end{bmatrix} + \varepsilon \begin{bmatrix} \bar{\mathbf{X}}^{[1]}(\mathbf{x},\phi) \\ \bar{\mathbf{\Omega}}^{[1]}(\mathbf{x},\phi) \\ 0 \end{bmatrix}, \tag{5}$$

Isotropy	Solution	Type
$\mathbf{Z}_2\times\mathbf{Z}_2$	$(x_1,x_2) = (0,0)$	Trivial
$\mathbf{Z}_2(1,-1)$	$(x_1,x_2) = \left(\sqrt{\frac{4(a-R_1)}{3b}},\ 0\right)$	Mode 1
$\mathbf{Z}_2(-1,1)$	$(x_1,x_2) = \left(0,\ \sqrt{\frac{4(a-R_2)}{3b}}\right)$	Mode 2
1	$(x_1,x_2) = (x_1^*,\ x_2^*)$	Mixed-Mode

TABLE I: Classification of solutions of Eq. (6) based on isotropy subgroups.

where

$$\begin{aligned} \bar{\mathbf{X}}^{[1]}(\mathbf{x},\phi) &= \frac{1}{(2\pi)^2}\int_{\mathbf{T}^2}\mathbf{X}^{[1]}(\mathbf{x},\phi,0)\ d\phi_1\ d\phi_2 \\ \bar{\mathbf{\Omega}}^{[1]}(\mathbf{x},\phi) &= \frac{1}{(2\pi)^2}\int_{\mathbf{T}^2}\mathbf{\Omega}^{[1]}(\mathbf{x},\phi,0)\ d\phi_1\ d\phi_2. \end{aligned}$$

After simplifying, we find that $\bar{\mathbf{\Omega}}^{[1]}(\mathbf{x},\phi) = (0,0)$, i.e., $\psi_1' = \psi_2' = 0$, so we can re-write the averaged system (5) more explicitly

$$\begin{aligned} x_1' &= \varepsilon(a-R_1)x_1 - \varepsilon\frac{3b}{4}\big(x_1^2 + 2x_2^2\big)x_1 \\ x_2' &= \varepsilon L_r(a-R_2)x_2 - \varepsilon L_r\frac{3b}{4}\big(x_2^2 + 2x_1^2\big)x_2 \\ \phi_1' &= \Omega_1 \\ \phi_2' &= \Omega_2. \end{aligned} \tag{6}$$

Details of the stability analysis of the solutions of Eq. (6) can be found in[2]. We now re-write Eq. (6) in complex form by letting $z_1 = x_1 e^{\phi_1 i}$ and $z_2 = x_2 e^{\phi_2 i}$.

$$\begin{aligned} \dot{z}_1 &= (\varepsilon\mu_1 + \Omega_1 i)z_1 - \varepsilon\frac{3b}{4}\big(|z_1|^2 + 2|z_2|^2\big)z_1 \\ \dot{z}_2 &= (\varepsilon\mu_2 + \Omega_2 i)z_2 - \varepsilon L_r\frac{3b}{4}\big(|z_2|^2 + 2|z_1|^2\big)z_2, \end{aligned} \tag{7}$$

where $\mu_1 = a - R_1$ and $\mu_2 = L_r(a - R_2)$. Observe that in these coordinates, Eq. (7) commutes with a 2-Torus $\mathbf{T}^2 = \mathbf{SO}(\mathbf{2})\times\mathbf{SO}(\mathbf{2})$, which acts on $\mathbf{R}^4 = \mathbf{C}^2$ diagonally by

$$(\theta_1,\theta_2)\cdot(z_1,z_2) = (e^{i\theta_1}z_1, e^{i\theta_2}z_2),$$

where $(\theta_1,\theta_2)\in\mathbf{T}^2$ and $(z_1,z_2)\in\mathbf{C}^2$. Observe also that the phase equations in (6) decouple from the amplitude equations due to the nonresonance conditions and they commute only with the standard action of the $\mathbf{Z}_2\times\mathbf{Z}_2$ symmetry group in the plane[13], which is what remains of the 2-torus $\mathbf{T}^2$ phase-shift symmetries.

This type of reflectional symmetry appears commonly in engineering applications of nonlinear oscillators. In

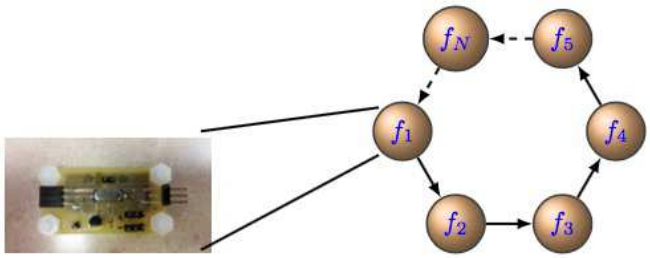

FIG. 2: CCOST concept with unidirectionally coupled crystal oscillators.

particular, it is found in classical systems such as: the pendulum equations[14], Duffing oscillators[15,16] and van der Pol oscillators[17–21]. In recent works, the same type of odd symmetry has appeared in moderns systems that include: vibratory gyroscopes[22–26] and energy harvesting systems[27,28]. We can now classify the four distinct type of solutions, i.e., steady states, periodic solutions, and invariant two-tori, of the original model Eq. (2) based on the isotropy subgroups of $\mathbf{Z}_2 \times \mathbf{Z}_2$. Table I provides a classification of all four solutions of Eq. (2) based on their isotropy subgroups.

The success of the averaging technique in the analysis of a single crystal oscillator model has lead us to consider a similar approach for the analysis of a network of coupled crystal oscillators. We discuss next the coupled system.

IV. COUPLED SYSTEM

In this section we consider a Coupled Crystal Oscillator System (CCOST) made up of N, assumed to be identical, crystal oscillators. We consider first the case of unidirectional coupling in a ring fashion, as is shown schematically in Fig. 2. Each node is represented by the circuit diagram found in Fig. 1. The spatial symmetry of the ring is described by the group $\mathbf{Z}_N$ of cyclic permutations of N objects. In the case of bidirectional coupling, the spatial symmetry is captured by the dihedral group $\mathbf{D}_N$ of permutations of an N-gon.

A. Governing Equations

Applying Kirchhoff's law to the CCOST network with unidirectional coupling yields the following governing equations

$$\begin{aligned} &L_{k,j}\frac{d^2 i_{k,j}}{dt^2} + R_{k,j}\frac{di_{k,j}}{dt} + \frac{1}{C_{k,j}} i_{k,j} = \\ &\left[a - 3b\big(i_{k,1} + i_{k,2} - \lambda\big[i_{k+1,1} + i_{k+1,2}\big]\big)^2\right] \\ &\left[\frac{di_{k,1}}{dt} + \frac{di_{k,2}}{dt} - \lambda\left(\frac{di_{k+1,1}}{dt} + \frac{di_{k+1,2}}{dt}\right)\right], \end{aligned} \tag{8}$$

where $k = 1, 2, \ldots, N \mod N$, $j = 1, 2$. Since we assume identical components in each crystal oscillator, then the set of parameters reduces to: $L_{k,1} = L_1$, $L_{k,2} = L_2$, $R_{k,1} = R_1$, $R_{k,2} = R_2$, $C_{k,1} = C_1$ and $C_{k,2} = C_2$. Letting $t = \sqrt{L_1 C_1}\tau$, $\Omega_1^2 = 1$, $\Omega_2^2 = \frac{L_1}{L_2}\frac{C_1}{C_2}$, $L_r = \frac{L_1}{L_2}$, $\varepsilon = \sqrt{\frac{C_1}{L_1}}$, and relabeling τ as time t, we write Eq. (8) in dimensionless form

$$\begin{aligned} &\frac{d^2 i_{k,1}}{dt^2} + \Omega_1^2 i_{k,1} = \\ &\varepsilon\left\{-R_1\frac{di_{k,1}}{dt} + \left[a - 3b\big(i_{k,1} + i_{k,2} - \lambda\big[i_{k+1,1} + i_{k+1,2}\big]\big)^2\right]\right. \\ &\left.\left[\frac{di_{k,1}}{dt} + \frac{di_{k,2}}{dt} - \lambda\left(\frac{di_{k+1,1}}{dt} + \frac{di_{k+1,2}}{dt}\right)\right]\right\} \\ &\frac{d^2 i_{k,2}}{dt^2} + \Omega_2^2 i_{k,2} = \\ &\varepsilon L_r\left\{-R_2\frac{di_{k,2}}{dt} + \left[a - 3b\big(i_{k,1} + i_{k,2} - \lambda\big[i_{k+1,1} + i_{k+1,2}\big]\big)^2\right]\right. \\ &\left.\left[\frac{di_{k,1}}{dt} + \frac{di_{k,2}}{dt} - \lambda\left(\frac{di_{k+1,1}}{dt} + \frac{di_{k+1,2}}{dt}\right)\right]\right\}. \end{aligned} \tag{9}$$

After applying the following set of invertible coordinates transformations

$$\begin{aligned} i_{kj} &= x_{kj}\cos\phi_{kj}; \\ i'_{kj} &= -\Omega_j x_{kj}\sin\phi_{kj}; \\ i''_{kj} &= -\Omega_j x'_{kj}\sin\phi_{kj} - \Omega_j^2 x_{kj}\cos\phi_{kj} - \Omega_j x_{kj}\psi'_{kj}\cos\phi_{kj}; \\ \phi_{kj} &= \Omega_j\, t + \psi_{kj}; \end{aligned} \tag{10}$$

for $j = 1, 2$ we arrive at the following set of equations, written symbolically as:

$$\begin{bmatrix} \mathbf{x}'_k \\ \phi'_k \end{bmatrix} = \begin{bmatrix} 0 \\ \mathbf{\Omega}^0 \end{bmatrix} + \varepsilon \begin{bmatrix} \mathbf{X}^{[1]}(\mathbf{x}_k, \phi_k, \phi_{k+1}, \varepsilon) \\ \mathbf{\Omega}^{[1]}(\mathbf{x}_k, \phi_k, \phi_{k+1}, \varepsilon) \end{bmatrix}, \tag{11}$$

where $\mathbf{x}_k = (x_{k1}, x_{k2})$, $\phi_k = (\phi_{k1}, \phi_{k2})$ and $\mathbf{\Omega}^0 = (\Omega_1, \Omega_2)$. The vector $\mathbf{X}^{[1]}$ has polynomial functions containing linear and cubic terms in x_{k1}, x_{k2}, $x_{k+1,1}$ and $x_{k+1,2}$ while $\mathbf{\Omega}^{[1]}$ has terms only dependent on ϕ_k and at most quadratic terms in $\mathbf{x}_{k+1}$ divided by $\mathbf{x}_k$.

Next we remove the $O(\varepsilon)$ dependence in the equation for ϕ_k by using coordinates $\phi_k \mapsto \phi_k + \phi_s$ and $\phi_{k+1} \mapsto \phi_{k+1} + \phi_s$, where $\phi_s = (\phi_{s1}, \phi_{s2})$. Then Eq. (11) becomes

$$\begin{bmatrix} \mathbf{x}'_k \\ \phi'_k \\ \phi'_s \end{bmatrix} = \begin{bmatrix} 0 \\ 0 \\ \mathbf{\Omega}^0 \end{bmatrix} + \varepsilon \begin{bmatrix} \mathbf{X}^{[1]}(\mathbf{x}_k, \phi_k + \phi_s, \phi_{k+1} + \phi_s, \varepsilon) \\ \mathbf{\Omega}^{[1]}(\mathbf{x}_k, \phi_k + \phi_s, \phi_{k+1} + \phi_s, \varepsilon) \\ 0 \end{bmatrix}. \tag{12}$$

The explicit form of these equations is shown in Appendix VIII.

In the bidirectional case, the dimensionless equations

are

$$
\begin{aligned}
&\frac{d^2 i_{k,1}}{dt^2} + \Omega_1^2 i_{k,1} = \\
&\varepsilon \Big\{ -R_1 \frac{di_{k,1}}{dt} + \big[a - 3b\big(i_{k,1} + i_{k,2} - \\
&\lambda\big[i_{k+1,1} + i_{k+1,2} + i_{k-1,1} + i_{k-1,2}\big]\ \big)^2\big] \\
&\Big[\frac{di_{k,1}}{dt} + \frac{di_{k,2}}{dt} - \\
&\lambda\left(\tfrac{di_{k+1,1}}{dt} + \frac{di_{k+1,2}}{dt} + \frac{di_{k-1,1}}{dt} + \frac{di_{k-1,2}}{dt}\right)\Big]\Big\} \\
&\frac{d^2 i_{k,2}}{dt^2} + \Omega_2^2 i_{k,2} = \\
&\varepsilon L_r \Big\{ -R_2 \frac{di_{k,2}}{dt} + \big[a - 3b\big(i_{k,1} + i_{k,2} - \\
&\lambda\big[i_{k+1,1} + i_{k+1,2} + i_{k-1,1} + i_{k-1,2}\big]\ \big)^2\big] \\
&\Big[\frac{di_{k,1}}{dt} + \frac{di_{k,2}}{dt} - \\
&\lambda\left(\tfrac{di_{k+1,1}}{dt} + \frac{di_{k+1,2}}{dt} + \frac{di_{k-1,1}}{dt} + \frac{di_{k-1,2}}{dt}\right)\Big]\Big\}.
\end{aligned}
\tag{13}
$$

The transformation (10) leads to the following network equations

$$
\begin{bmatrix} \mathbf{x}_k' \\ \phi_k' \\ \phi_s' \end{bmatrix} = \begin{bmatrix} 0 \\ 0 \\ \mathbf{\Omega}^0 \end{bmatrix} + \varepsilon \begin{bmatrix} \mathbf{X}^{[1]}(\mathbf{x}_k, \phi_k + \phi_s, \phi_{k+1} + \phi_s, \phi_{k-1} + \phi_s \varepsilon) \\ \mathbf{\Omega}^{[\mathbf{1}]}(\mathbf{x}_k, \phi_k + \phi_s, \phi_{k+1} + \phi_s, \phi_{k-1} + \phi_s \varepsilon) \\ 0 \end{bmatrix} \tag{14}
$$

with $\mathbf{X}^{[1]}$ is a vector of polynomial functions containing linear and cubic terms in x_{k1}, x_{k2}, $x_{k+1,1}$, $x_{k+1,2}$, $x_{k-1,1}$ and $x_{k-1,2}$ and $\mathbf{\Omega}^{[\mathbf{1}]}$ has a similar structure as described above. The complete set of equations is shown in Appendix VIII.

We now write explicitly the averaged equations for a network of crystal oscillators coupled unidirectionally. We rescale time by $\tau = \varepsilon t$ and the amplitude dynamics are

$$
\begin{aligned}
\dot{x}_{k1} &= (a - R_1) x_{k1} - \frac{3}{4} b (x_{k1}^2 + 2x_{k2}^2) x_{k1} - \frac{3}{2} b\lambda^2 (x_{k+1,1}^2 + x_{k+1,2}^2) x_{k1} - a\lambda\, x_{k+1,1} \cos\alpha_{k1} + \\
&\quad \frac{3}{4} b\lambda\, (3x_{k1}^2 + 2x_{k2}^2) x_{k+1,1} \cos\alpha_{k1} + 3\, b\lambda\, x_{k1} x_{k2} x_{k+1,2} \cos\alpha_{k2} - \frac{3}{4} b\lambda^2 x_{k1} x_{k+1,1}^2 \cos 2\alpha_{k1} - \\
&\quad \frac{3}{2} b\lambda^2 x_{k2} x_{k+1,1} x_{k+1,2} \left(\cos(\alpha_{k1} + \alpha_{k2}) + \cos(\alpha_{k1} - \alpha_{k2})\right) + \frac{3}{4} b\lambda^3 (x_{k+1,1}^2 + 2x_{k+1,2}^2) x_{k+1,1} \cos\alpha_{k1} \\
\dot{x}_{k2} &= L_r (a - R_2) x_{k2} - \frac{3}{4} L_r b (x_{k2}^2 + 2x_{k1}^2) x_{k2} - \frac{3}{2} L_r b\lambda^2 (x_{k+1,1}^2 + x_{k+1,2}^2) x_{k2} - L_r a\lambda\, x_{k+1,2} \cos\alpha_{k2} + \\
&\quad \frac{3}{4} L_r b\lambda\, (3x_{k2}^2 + 2x_{k1}^2) x_{k+1,2} \cos\alpha_{k2} + 3\, L_r b\lambda\, x_{k1} x_{k2} x_{k+1,1} \cos\alpha_{k1} - \frac{3}{4} L_r b\lambda^2 x_{k2} x_{k+1,2}^2 \cos 2\alpha_{k2} - \\
&\quad \frac{3}{2} L_r b\lambda^2 x_{k1} x_{k+1,1} x_{k+1,2} \left(\cos(\alpha_{k1} + \alpha_{k2}) + \cos(\alpha_{k1} - \alpha_{k2})\right) + \frac{3}{4} L_r b\lambda^3 (x_{k+1,2}^2 + 2x_{k+1,1}^2) x_{k+1,2} \cos\alpha_{k2},
\end{aligned}
$$

where $\alpha_{k1} = \phi_{k1} - \phi_{k+1,1}$ and $\alpha_{k2} = \phi_{k2} - \phi_{k+1,2}$. Similarly, the phase dynamics are

$$
\begin{aligned}
x_{k1}\dot{\phi}_{k1} &= a\lambda\, x_{k+1,1} \sin\alpha_{k1} - \frac{3}{4} b\lambda\, (x_{k1}^2 + 2x_{k2}^2) x_{k+1,1} \sin\alpha_{k1} + \frac{3}{4} b\lambda^2 x_{k1} x_{k+1,1}^2 \sin 2\alpha_{k1} - \\
&\quad \frac{3}{4} b\lambda^3 (x_{k+1,1}^2 + 2x_{k+1,2}^2) x_{k+1,1} \sin\alpha_{k1} + \frac{3}{2} b\lambda^2 x_{k2} x_{k+1,1} x_{k+1,2} \left(\sin(\alpha_{k1} + \alpha_{k2}) + \sin(\alpha_{k1} - \alpha_{k2})\right) \\
x_{k2}\dot{\phi}_{k2} &= L_r a\lambda\, x_{k+1,2} \sin\alpha_{k2} - \frac{3}{4} L_r b\lambda\, (x_{k2}^2 + 2x_{k2}^2) x_{k+1,2} \sin\alpha_{k2} + \frac{3}{4} L_r b\lambda^2 x_{k2} x_{k+1,2}^2 \sin 2\alpha_{k2} - \\
&\quad \frac{3}{4} L_r b\lambda^3 (x_{k+1,2}^2 + 2x_{k+1,1}^2) x_{k+1,2} \sin\alpha_{k2} + \frac{3}{2} L_r b\lambda^2 x_{k1} x_{k+1,1} x_{k+1,2} \left(\sin(\alpha_{k1} + \alpha_{k2}) + \sin(\alpha_{k1} - \alpha_{k2})\right)
\end{aligned}
$$

A similar set of equations are obtained for the bidirectional case. The complete equations are omitted for brevity as they are very long, but they are found in[2]. The symmetry of these averaged amplitude-phase equations is captured by the groups $\mathbf{Z}_N \times \mathbf{O}(\mathbf{2}) \times \mathbf{O}(\mathbf{2})$ and $\mathbf{D}_N \times \mathbf{O}(\mathbf{2}) \times \mathbf{O}(\mathbf{2})$ for the unidirectional and bidirectional coupling cases, respectively. A complete analysis of the equations can be found in[2]. We summarize the main results. Steady-states of the averaged system with symmetry group $\Sigma \subset \Gamma \times \mathbf{SO}(\mathbf{2})$, with $\Gamma = \mathbf{Z}_N$ and $\Gamma = \mathbf{D}_N$ lead to periodic solutions with spatio-temporal symmetry $\Sigma \subset \Gamma \times \mathbf{S}^1$. Then, the tangent space to the trivial steady-state can be decomposed along irreducible representations of the $\mathbf{Z}_N$ and $\mathbf{D}_N$ actions and thus we obtain a block diagonalization of the linearization of the complexified governing equations. Symmetry-preserving and symmetry-breaking bifurcations are then determined by examining the eigenvalues computed directly from the block diagonalization. Criticality computations are also performed to determine the direction of bifurcations.

V. PHASE ERROR

Phase error is defined as the drift of the period of oscillation of an oscillating system away from the expected period length. Reducing this phase error will allow a potential network-based precision timing device to produce more accurate time measures, and with a longer duration. In order to simulate phase error in the proposed CCOST system, Eq. (12) and Eq. (14) must be cast as a stochastic model, with colored noise added to simulate fluctuations due to electronic components–that is, the noise is assumed to be Gaussian, band-limited, having a zero mean, a variance σ^2, and have a specific correlation time, τ_c. The noise is assumed to not drive the dynamics of the system, this corresponds to $\tau_f \ll \tau_c$, where τ_f is the time-constant of each oscillator[29,30]. These assumptions lead us to re-write Eq. (12) and Eq. (14) together in a more general Langevin form:

$$\begin{aligned} d_t X_k &= F(X_k) - \lambda \sum_{j \to k}^{N} h(X_j, X_k) + \eta_k \\ d_t \eta_k &= -\frac{\eta_k}{\tau_c} + \frac{\sqrt{2D}}{\tau_c}\xi_k, \end{aligned} \tag{15}$$

where $X_k = [i_{k1}, i'_{k1}, i_{k2}, i'_{k2}]$ is the state variable of each crystal oscillator, τ_c, D are correlation time and intensity respectively, F represents the internal dynamics of each oscillating unit, i.e., each crystal oscillator as is described by Eq. (1), h is the coupling function between two oscillators, in which the summation is taken over those cells j that are coupled to each cell k, λ is the (assumed to be identical) coupling strength, and each η_k describes the noise function applied to the kth oscillator, ξ_k is a Gaussian distributed random variable with zero mean, and standard deviation σ. Each colored noise function is characterized by $\langle \eta_i(t) \rangle = 0$ and $\langle \eta_i(t)\eta_j(s) \rangle = (D/\tau_c) \times \exp[-|t-s|/\tau_c]$, where $D = \sigma^2\tau_c^2/2$[31]. As $\tau_c \to 0$ the noise becomes white, however in practice all noise is band limited[32]. For the purpose of our simulations, $\tau_c = 1 \times 10^{-3}$ and $D = 5 \times 10^5$.

The model Eq. (15) is numerically integrated using the Euler-Maruyama scheme[29]. Since the stochastic process in Eq. (15) is additive and independent of the solution X, more advanced stochastic numerical schemes, like the Milstein method, reduce to Euler-Maruyama[33]. Figure 3 illustrates a typical solution of this stochastic model with strong positive coupling, where $N = 3$. Note that only one noise function is plotted. In these simulations, we raised the resistance parameter R_2 from 181.1Ω (in[2]) to 1000Ω. This change forces the model outside of the parameter space in which the 66MHz solution (the parasitic oscillation) exists. The high frequency solution is removed because, this solution is not dominant in the physical experiments.

Phase error is calculated by first locating the zeros of each individual solution X_k, i.e., each oscillatory node in the network. The zeros are approximated using a standard three point quadratic interpolation method. From the location of the zeros, the periods of oscillation are calculated. Let $P_k = \{p_{ki}\}_{i=1}^{n}$ be the sequence of periods of solution X_k, and σ_p be the mean absolute deviation of the periods. Then phase error in the k^{th} component of the collective network oscillation is defined as

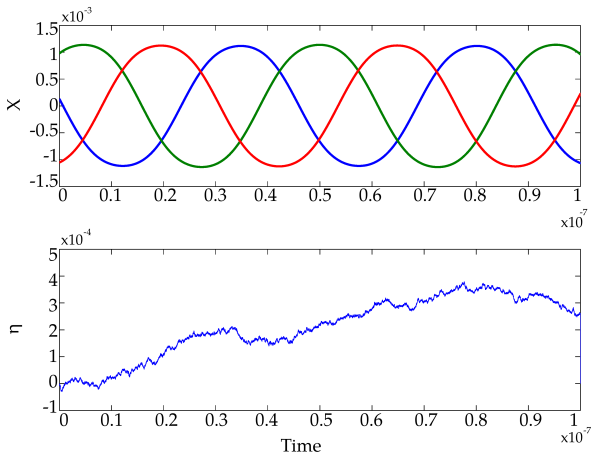

FIG. 3: This figure displays 22MHz rotating wave solution, RW_1^1, of the unidirectional CCOST model, with 3 nodes and coupling strength $\lambda = 0.99$. (Top) The current, X_i, is plotted over a period of 1.0×10^{-7} seconds. (Bottom) Noise function is displayed over the same duration.

$$\text{Phase Error}_k = \frac{\sigma_{P_k}}{E(P_k)}$$

where σ_{P_k} is the mean absolute deviation of the periods P_k and $E(P_k)$ is the expected period length. Under normal conditions the standard deviation is normally used for phase error; however due to the natural length of the periods, the squared error for each period is smaller than machine epsilon leaving those measurements unreliable. The mean absolute deviation does not square the values so that the calculations stay away from machine epsilon, $\mathcal{O}(1 \times 10^{-16})$. Phase error in the work is then computed by averaging out the phase error of all individual units

$$\text{Phase Error}_{Network} = \frac{1}{N}\sum_{k=1}^{N} \text{Phase Error}_k \tag{16}$$

When noise is removed from the equation the phase error is 0. The size of the sequence of periods is dictated by the saved integration time. The integration time used for the data sets considered in this paper was 3.5×10^{-5} seconds. The corresponding period for the 22MHz solution is approximately 4.5×10^{-8} sec. Therefore, the phase error is the sample standard deviation of approximately 778 cycles. The data presented in the following sections displays the mean phase error for 50 simulations for each value of N. The simulation samples were calculated and

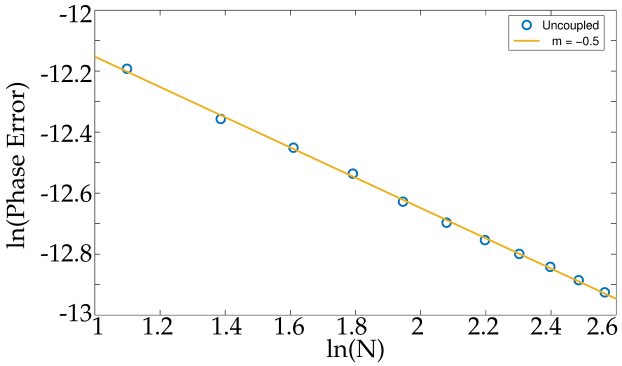

FIG. 4: The uncoupled-averaged ($\lambda = 0$) log scaled phase error as a function of array size. This figure displays the average taken over 50 samples for each N. A least squares regression line shows that the scaling exponent is -0.5, corresponding to a phase error reduction of $1/\sqrt{N}$.

collected utilizing the High Performance Computing Center (HPC) at SPAWAR Systems Center Pacific, Naval Base Point Loma in San Diego, California. Correlation time, τ_c, of the additive noise does not affect the computation of phase error as long as it is significantly larger that the time constant τ_f of each oscillator, so the that collective behavior is not driven purely by noise.

A. Uncoupled Control Group

Naturally, the performance of an ensemble of uncoupled oscillator system will serve as a baseline to compare the performance of the patterns generated by the coupling topology in a CCOST system. Observe that the uncoupled model is a reduction of Eq. (15) when $\lambda = 0$. At the United States Naval Observatory, it has been observed that an averaged time signal collected from an (uncoupled) ensemble of atomic clocks has a phase error reduction of approximately $1/\sqrt{N}$, where N is the number of oscillators in the particular system. Figure 4 illustrates the simulation test of the uncoupled ensemble.

Each point is the average of 50 simulations. The log scaled phase error is fitted with a least squares regression. This line shows that the reduction follows a scaling exponent of -0.5, a $1/\sqrt{N}$ curve in normal space, consistent with the measurements at the Naval Observatory. The uncoupled simulation serves as a baseline to compare the performance of the patterns induced by coupling.

B. Unidirectional Coupling

We consider the model equation under the unidirectional topology, that is, when the coupling function is of the form $h(X_j, X_k) = h(X_k, X_{k+1})$. Specifically, the governing equations become:

$$\begin{aligned} d_t X_k &= F(X_k) - \lambda h(X_k, X_{k+1}) + \eta_k \\ d_t \eta_k &= -\frac{\eta_k}{\tau_c} + \frac{\sqrt{2D}}{\tau_c}\xi_k, \end{aligned} \tag{17}$$

for all $k = 1, \ldots, N$, again where N is the total number of oscillators in the system. All other parameters are the same as in Eq. (15). This network experiences different patterns of oscillation depending on the strength of the coupling parameter, λ. Notably, there are three patterns of interest: a rotating wave solution where each consecutive node is T/N out of phase (denoted RW_1), a rotating wave where every other node is $T/2$ out of phase (when N is even), where even and odd nodes are synchronized (denoted RW_2), and a fully synchronized pattern. Both rotating waves exist and are stable when $\lambda > 0$. In the parameter regime of our simulations, the pattern RW_1 is stable for odd N, whereas the pattern RW_2 exists only when N is even. The synchronized pattern is stable when $\lambda < 0$. This subsection illustrates which pattern has the best phase error reduction. Detailed information on the nature of the symmetry-breaking bifurcations that lead to the emergence of patterns, and their stability, for both the unidirectional and bidirectional networks can be found in[2].

A sorting algorithm was developed to separate phase error values depending on which pattern was observed. This algorithm finds the first peak of each oscillator in the system, after transient integration, and calculates the time difference between them. For example, let $N = 3$, ϵ be a specified tolerance, and T be the expected period. If $t_d = |t_{peak(i)} - t_{peak(i+1)}|$ and $t_d - T/3 < \epsilon$, for each $i \leq N - 1$, then the algorithm sorts the pattern as RW_1, the T/N rotating wave. However, if $t_d < \epsilon$ for all $i < N$, then the algorithm sorts the pattern as synchronized.

Figure 5 is composed of the logarithmic scaled data and their respective least squares regression line. The purple circles are the data points for the synchronized pattern. The simulation of this pattern shows that the phase error data best fits a scaling exponent, m, of $m = -0.4868$ close to the uncoupled performance. The blue data points shows the phase error reduction for the standard rotating wave RW_1. This pattern best fits a scaling exponent of $m = -0.9716$, performing better than the uncoupled ensemble and closely resembling a $1/N$ phase error reduction. The green data points show the performance of the rotating wave RW_2. This pattern performs much like the synchronized solution with a scaling exponent of $m = -0.4736$.

The previous results presented so far represent a sample of phase errors for specific values of coupling strength, i.e., $\lambda = -0.99$ for synchronized solutions, $\lambda = 0$ for uncoupled ensemble, and $\lambda = 0.99$ for rotating waves. Since there is a significant variation between the uncoupled scaling and the scaling for RW_1, the phase error analysis was expanded to examine the phase reduction along the interval $0 < \lambda < 0.99$. Figure 6 illustrates the

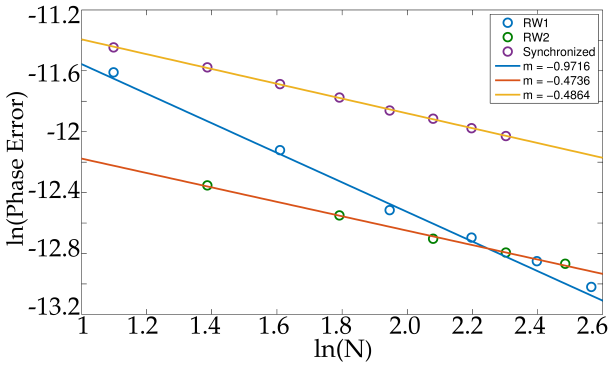

FIG. 5: The log scaled phase errors for the synchronized, the T/N rotating wave, and the $T/2$ rotating wave solutions. $\lambda = -0.99$ for the synchronized solution and $\lambda = 0.99$ for the rotating waves. This figure displays the average of 50 samples taken for each N. A least squares regression is fitted to the logged data to illustrate the scaling exponent, m, of each pattern.

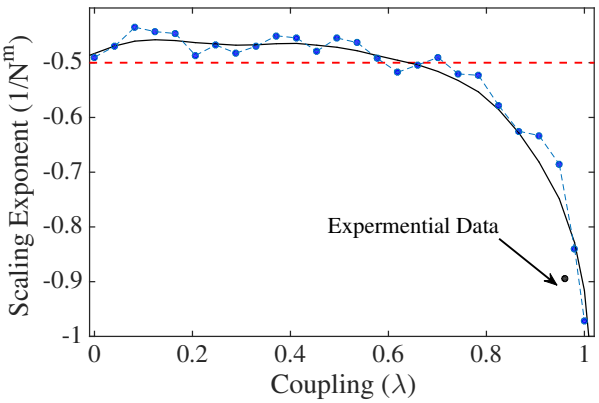

FIG. 6: Phase error scaling for the RW_1 pattern as a function of λ such that $\lambda \in (0, 1)$, with dashed lines indicating $1/\sqrt{N}$ and $1/N$ scalings.

performance with respect to the scaling exponent, i.e., this figure is a log plot phase error, $Err(N, \lambda) = N^{m(\lambda)}$. Samples are taken for 100 values of λ. For each value of λ, the mean phase error for 50 repeated simulations is calculated for $N = 3, 5, \ldots, 21$. Then a least squares regression is performed on the log of these values, producing the scaling exponents depicted in Fig 6. This analysis suggests that strong coupling is preferable to weak coupling to produce optimal scaling. From Fig 6, the optimal scaling is found at $\lambda = 0.99$ with $m = -0.8947$. Notice that for $\lambda \in (0, 0.387)$, the coupled system performs poorly compared to the uncoupled standard, having a scaling exponent $m(\lambda) > -0.5$. When the circuit is coupled the inherent noise of each node is amplified by the coupling, and in the case of $0 < \lambda < 0.387$ the coupling is too

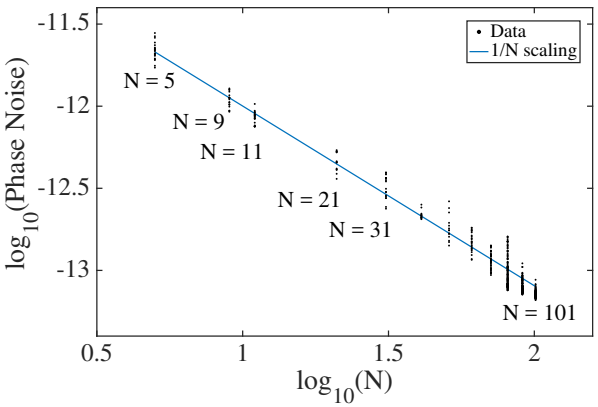

FIG. 7: Phase error scaling for a larger number of oscillators in an unidirectionally coupled array. Coupling strength is held fixed at $\lambda = 0.95$. The observed variations from the $1/N$ scaling are due to transient behavior in the system.

weak to overcome the amplification in noise. For values of coupling strength in the interval $\lambda > 1$, all traveling wave patterns and discrete rotating waves are unstable, so they could not be used in an actual CCOST device and we do not need to consider them in here.

In order to obtain more statistically meaningful results of scaling law, we conducted additional simulations of the unidirectionally coupled network with larger values of N. The simulations are very time consuming. Thus, instead of sweaping through the entire range of values of coupling strength, we held the coupling strength fixed, and near the region of strong strength, i.e., near $\lambda = 1.0$. Figure 7 shows that phase drift error still follows, approximately, a $1/N$ scaling law. The observed variations, mainly for large values of N, are due to transient behavior in the simulations. That is, as N increases, the transient time that we must wait until collecting phase drift data must increase significantly. But this also increases the time it takes to run the simulations, thus a tradeoff choice must be made to be able to report results in a timely manner.

From a physics standpoint we can explain the observed results of phase drift by examining the phase relations among nearest neighbor oscillators. Consider a generic pattern of oscillation described as

$$X(t) = \left(i_1\left(t + k_1\tfrac{T}{N}\right), i_1\left(t + k_2\tfrac{T}{N}\right), i_1\left(t + k_3\tfrac{T}{N}\right), i_1\left(t + k_4\tfrac{T}{N}\right), \ldots, i_1\left(t + k_N\tfrac{T}{N}\right)\right).$$

The standard traveling wave pattern corresponds to $k_1 = 0, k_2 = 1, \ldots, k_N = N - 1$. Discrete rotating waves would follow a different sequence. For instance, with $N = 5$, a commonly observed wave is one in which the phase difference skips one oscillator at a time, it has the form

$$X(t) = (i_1(t), i_1(t + 3T/5), i_1(t + T/5), i_1(t + 4T/5), i_1(t + 2T/5)).$$

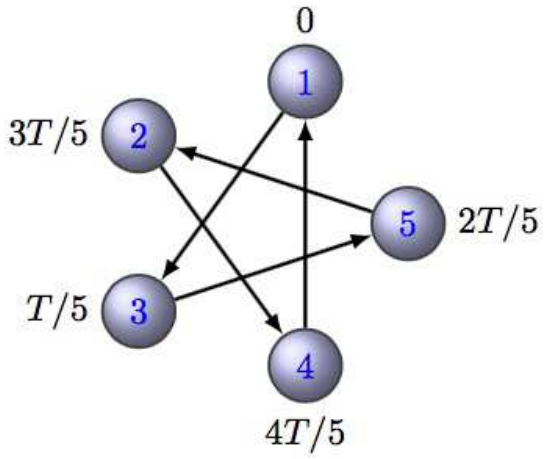

FIG. 8: Discrete rotating wave predicted by symmetry-breaking Hopf bifurcations in a network of five crystal oscillators coupled unidirectionally.

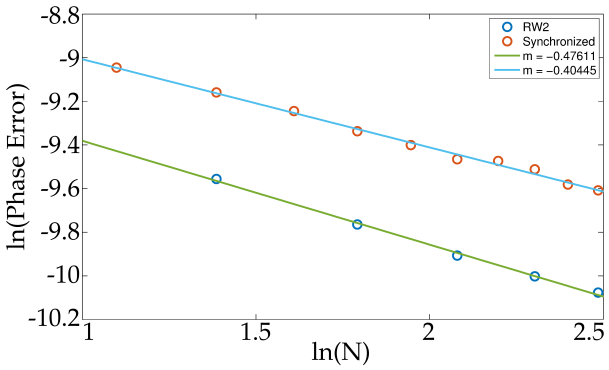

FIG. 9: Log scale phase error for the synchronized and RW_2 solutions in a bidirectionally coupled ring. The average of 50 simulations is plotted for each value of N. The synchronized solution performs slightly worse than the uncoupled scaling, while the RW_2 pattern is fitted to a reduction exponent of $m - 0.47611$.

This discrete rotating wave corresponds to $k_1 = 0$, $k_2 = 3$, $k_3 = 1$, $k_4 = 4$, and $k_5 = 2$. Observe that the constant phase difference of $T/5$ follows the following order of the oscillators: $1, 3, 5, 2, 4$. The pattern can be easily visualized with the aid of Fig. 8. Notice that it is also possible for the phase difference to skip two oscillators instead of one. However, this would lead to a similar rotating wave oscillating in the opposing direction, i.e., a conjugate pattern. But for larger arrays it is quite possible for a discrete rotating wave to have phase differences that skip a larger number of oscillators. As the number of oscillators that are skipped increases, the coherence between nearest neighbors is reduced so that the network tends to behave more as an "uncoupled" array and, consequently, the phase drift converges toward that of an uncoupled ensemble. On the other hand, in the standard traveling wave pattern, nearest neighbors have the smallest phase difference and phase drift decreases. In future work, we expect to follow this line of thought to provide a mathematical proof for the scaling law by taking into account the phase difference between nearest neighbors.

C. Bidirectional Coupling

We now consider Eq. (15) under the bidirectional topology, that is, when the coupling function is of the form $h(X_j, X_k) = h(X_{k-1}, X_k, X_{k+1})$. Specifically, the governing equations become:

$$\begin{aligned} d_t X_k &= F(X_k) - \lambda h(X_{k-1}, X_k, X_{k+1}) + \eta_k \\ d_t \eta_k &= -\frac{\eta_k}{\tau_c} + \frac{\sqrt{2D}}{\tau_c}\xi_k, \end{aligned} \tag{18}$$

for all $k = 1, \ldots, N$, again where N is the total number of oscillators in the system. All other parameters are the same as in Eq. (15). The bidirectional topology yields two generically stable patterns. The synchronized solution for $\lambda \in (-0.5, 0)$ and the RW_2 solution where each node is $T/2$ out of phase, appearing when $\lambda \in (0, 0.5)$ and N is even. The numerical computations in[2] suggest that for $\lambda > 0$ and N odd, there are no stable patterns. Figure 9 illustrates phase error diagrams for both patterns in the bidirectional coupling scheme. Interestingly, the synchronized state seems to have a worse scaling than the averaged uncoupled case, whereas the pattern RW_2 matches both the uncoupled and it's unidirectional counterpart with a close to $1/\sqrt{N}$ scaling.

VI. PRELIMINARY EXPERIMENTS

A system of coupled crystal oscillators are being constructed and tested at the nonlinear dynamics laboratory at Space and Naval Warfare Systems Center Pacific, San Diego, California. Programmable Integrated Circuits were used as designing blocks for fabricating networks of coupled crystal oscillators. They are essentially computers with a crystal clock inside to synchronize flow of data. They are found in alarm systems, phones, in fact almost any electronic device. They can be programmed to control a production line or, in our case, to be timers. The experimental CCOST design has a base clock of 32 KHz. This is achieved through the choice of RLC components, so that only one mode oscillates at 32 KHz while the other (parasitic) mode is unstable. Furthermore, the condition on correlation time of noise being significantly larger than the time constant of the oscillators guarantees that the network dynamics is not driven purely by noise, so noise-induced switching between modes of oscillation

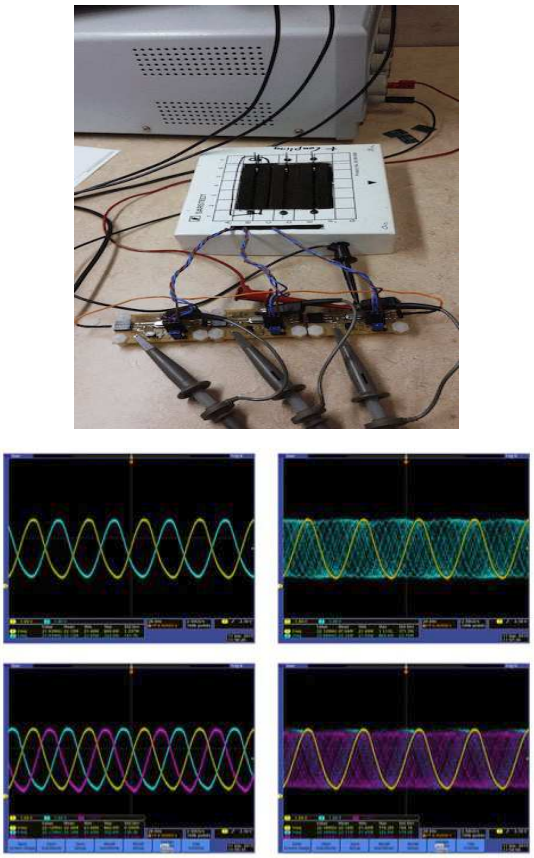

FIG. 10: (Top) Experimental realization of a network of coupled crystal oscillators implemented via PIC boards. Each PIC board includes the oscillator circuitry and a port for coupling to create a network. RLC components guarantee that one mode oscillates at the desired frequency of 32 KHz while the other (parasitic) mode is unstable. The external small box contains the potentiometer to control the gain of the operational amplifiers and, in this way, manipulate the desired coupling strength across the network. (Bottom-left) Experimental measurements for $N = 2$ and $N = 3$ reveal, as expected, a traveling wave pattern among the oscillations. (Bottom-right) When the oscillators are uncoupled the pattern disappears.

can be prevented. And even for (uncommonly) larger values of noise, the system would eventually switch back to the desired mode of oscillation as soon as the noise levels would decrease to more normal values. Recall also that a major reason for the wide use of crystal oscillators is their high Q factor. Higher Q indicates a lower rate of energy loss relative to the stored energy of the resonator; the oscillations die out more slowly. Figure 10(top) illustrates the design and network response captured by an oscilloscope. The white box in the figure contains appropriate potentiometers to control the gain of the operational amplifiers, which in turn, are used to manipulate coupling strength, and thus, control the network response to the desired pattern of oscillation.

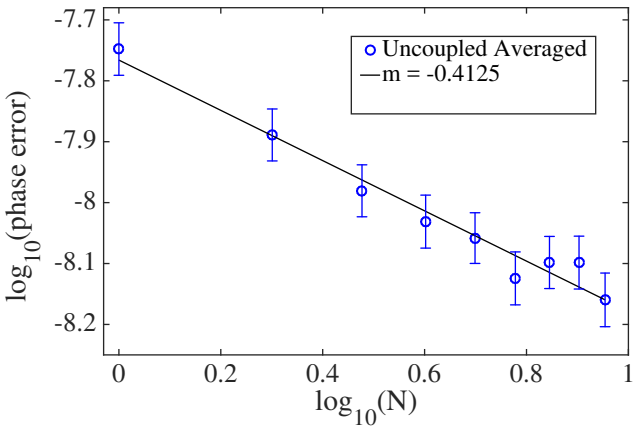

FIG. 11: Experimental phase error measured by averaging the phase error of a control group, i.e., an uncoupled ensemble of experimental crystal oscillators. The data points are plotted as well as least squares regression. The experimental phase error shows a reduction exponent of $m = -0.41254$.

Data from the experimental device was retrieved using the BI220 Time Interval Analyzer. This time analyzer has a measuring threshold of 8ps, and a maximum measurable frequency of 2.5 GHz[34]. For comparison purposes, an uncoupled control group of crystal oscillators rated at 32 KHz was also examined and phase error data extracted. Figure 11 illustrates the data collected from this experiment. The figure is plotted using a base 10 log scale. The data shows that the scaling exponent for the uncoupled control group is $m = -0.41254$.

Figure 12 illustrates now preliminary results from the experimental 32 KHz CCOST device with unidirectional coupling. Coupling strength in the experiment is tuned up to operate the device over the region where the RW_1 traveling pattern becomes stable. The data provided best fits a scaling exponent of $m = -0.8947$, which is relatively close to the expected $1/N$ scaling law predicted by the numerical simulations. Additional experiments are necessary to further investigate the robustness of the CCOST device. Those experiments and additional testing are all part of ongoing work, which we expect to report in future publications.

VII. DISCUSSION

This manuscript investigates the effects of colored noise on a network of N identical nonlinear crystal oscillators coupled together, either unidirectionally or bidirectionally, in a ring configuration. The robustness of the unidirectional and bidirectional networks under additive noise was investigated focusing on phase error. The primary interest was the scaling of the phase error reduction. We discovered that the unidirectionally coupled network preformed better than the uncoupled control in terms of

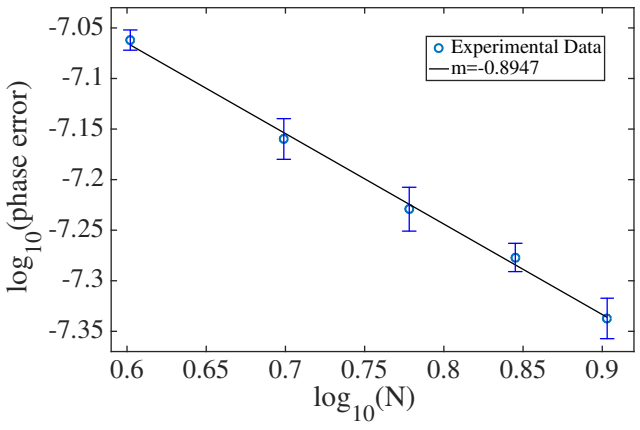

FIG. 12: Experimental phase error for a unidirectional CCOST device with the RW_1 pattern selected on a log 10 scale. The scaling exponent from the experimental data is $m = -0.8947$.

phase error reduction. However, not all of the patterns contained in the unidirectional coupling do. Indeed, a standard discrete rotating wave pattern, in which consecutive crystals oscillate out of phase by $2\pi/N$, performed better than other patterns and, significantly better that the average of an uncoupled ensemble. If one wanted to decrease the phase error by a factor of ten, one would simply need to couple ten more oscillators and induce them to oscillate in a similar traveling wave pattern. For comparisons purposes, to obtain a similar phase error reduction with an uncoupled ensemble, it would be necessary to average out the phase of about 100 oscillators. The tradeoff between uncoupled and coupled networks then becomes obvious. As the number of oscillators, N, grows to be large, coupling becomes less expensive than averaging.

Preliminary results from corresponding experiments support the results of the analysis and simulations. In fact, even with the slow circuits, a close to $1/N$ scaling law of phase error is readily obtained with a coupling circuitry. The experimental device was constructed using a solderless breadboard, and had variation within components. When an integrated circuit is constructed, we expect the components will be closer to uniform and the phase error scaling values will better align to the ones predicted in simulation. Further, when the device is fully developed, SPAWAR will be able to test the device against the Precise Intermediate-term Computer-controlled Oscillator (PICO) advanced clock, an averaged crystal oscillator device that is corrected by central processing units and low pass filters [35]. The PICO advanced clock was another precision timing solution that had been examined in the past. Overall, further experiments and testing are needed to investigate the fundamental limit of phase error reduction as N increases to very large values. However, in experiments with uncoupled and coupled topologies, the phase error scaling is slightly less than what is observed in simulations.

The emphasis of this work is on homogeneous networks of crystal oscillators, coupled instantaneously. This emphasis is not exhaustive by any means but it serves to identify directions and tasks for future work. One immediate task involves an analysis of the effects of delay. Indeed, while the mathematical model equations of the network of crystal oscillators assume instantaneous coupling, in practice we must account for the fact that even high-speed, high-precision, circuit components can introduce a delay in the coupling signal. Similarly, we expect uncertainty in networks of crystal oscillators to arise from two sources: fluctuations in parameter values due to material imperfections (inductances, resistors and capacitances) and signal contamination due to noise in the electronics. The former case may lead to non-homogeneities in parameters, which, in turn, translates into differences in the internal dynamics of each crystal oscillator. Thus, it is also important that we consider the effects of non-homogeneous electronic components.

The coupling type studied in this paper is simple additive coupling. Other forms of coupling could also be studied. For example, the coupling parameter could be a function of X_k and its neighbors, that is $\lambda = \lambda(X)$. There are a multitude of ways to couple electronic circuits such as, direct coupling, magnetic field coupling, power coupling and many more. The additive coupling presented in this paper, models direct signal coupling of electrical circuits. The CCOST device is being developed using direct coupling because the coupling strength in this strategy is more easily controlled. Coupling strategies such as power or magnetic field coupling are not easily controlled by the user. However, different coupling strategies may prove to have better phase error reduction and stability properties, than the one presented here. Additionally, the pattern analysis in[2] is oscillator independent. Some future work would be to examine the phase error reduction in other oscillator systems, such as using a Colpitts oscillator as the base node. These types of oscillators can offer additional advantages not found in crystals. For instance, one immediate advantage is that they do not require the use of crystals to oscillate, so implementation in an integrated circuit can be done inside a single silicon layer, as opposed to crystals that have to externally connected. In addition, they can also be tuned up to oscillate over a wide frequency spectrum, whereas the frequency of oscillation of crystals is predetermined by how they are cut and mounted, so their frequency can only be slightly adjusted. However, in order to obtain a high Q factor in Colpitts, they may have to be fabricated over a preferred frequency. These tradeoffs will have to be examined in more detail as part of future work.

Finally, other symmetric coupling schemes should also be taken into consideration. Under new symmetries, different patterns of collective behavior may emerge with different conditions for their existence and stability. All of these tasks are part of ongoing work with the ulti-

mate goal of guiding the design rules and operation of a precision timing device.

VIII. ACKNOWLEDGEMENT

We acknowledge support from ONR Code 30. A.P. was supported by DoD Office of Naval Research Grant N00014-16-1-2134. PLB (Discovery Grant) and CD (USRA) acknowledge funding from NSERC Canada.

Appendix A: Averaged Equations for Unidirectional Coupling

$$\begin{aligned}\dot{x}_{k,1} = -\frac{\epsilon}{\Omega_1}\,\sin(\phi_{k1}+\phi_{s1})\Big[&R_1 x_{k,1}\Omega_1\sin(\phi_{k1}+\phi_{s1})+\\ &\Big(a-3\,b\,\big(x_{k,1}\cos(\phi_{k1}+\phi_{s1})+x_{k,2}\cos(\phi_{k2}+\phi_{s2})-\lambda\,\big(x_{k+1,1}\cos(\phi_{k+1,1}+\phi_{s1})+\\ &x_{k+1,2}\cos(\phi_{k+1,2}+\phi_{s2})\big)\big)^2\Big)\Big(-\Omega_1 x_{k,1}\sin(\phi_{k1}+\phi_{s1})-\Omega_2 x_{k,2}\sin(\phi_{k2}+\phi_{s2})+\\ &\lambda\,\big(\Omega_1 x_{k+1,1}\sin(\phi_{k+1,1}+\phi_{s1})+\Omega_2 x_{k+1,2}\sin(\phi_{k+1,2}+\phi_{s2})\big)\Big)\Big],\end{aligned} \tag{A1}$$

$$\begin{aligned}\dot{x}_{k,2} = -\frac{\epsilon}{\Omega_2}\,L_r\sin(\phi_{k2}+\phi_{s2})\Big[&R_2\Omega_2 x_{k,2}\sin(\phi_{k2}+\phi_{s2})+\\ &\Big(a-3\,b\,\big(x_{k,1}\cos(\phi_{k1}+\phi_{s1})+x_{k,2}\cos(\phi_{k2}+\phi_{s2})-\lambda\,\big(x_{k+1,1}\cos(\phi_{k+1,1}+\phi_{s1})+\\ &x_{k+1,2}\cos(\phi_{k+1,2}+\phi_{s2})\big)\big)^2\Big)\Big(-\Omega_1 x_{k,1}\sin(\phi_{k1}+\phi_{s1})-\Omega_2 x_{k,2}\sin(\phi_{k2}+\phi_{s2})+\\ &\lambda\,\big(\Omega_1 x_{k+1,1}\sin(\phi_{k+1,1}+\phi_{s1})+\Omega_2 x_{k+1,2}\sin(\phi_{k+1,2}+\phi_{s2})\big)\Big)\Big],\end{aligned} \tag{A2}$$

$$\begin{aligned}\dot{\phi}_{k1} = -\frac{\epsilon}{\Omega_1 x_{k,1}}\,\cos(\phi_{k1}+\phi_{s1})\Big[&R_1 x_{k,1}\sin(\phi_{k1}+\phi_{s1})+\\ &\Big(a-3\,b\,\big(x_{k,1}\cos(\phi_{k1}+\phi_{s1})+x_{k,2}\cos(\phi_{k2}+\phi_{s2})-\lambda\,\big(x_{k+1,1}\cos(\phi_{k+1,1}+\phi_{s1})+\\ &x_{k+1,2}\cos(\phi_{k+1,2}+\phi_{s2})\big)\big)^2\Big)\Big(-\Omega_1 x_{k,1}\sin(\phi_{k1}+\phi_{s1})-\Omega_2 x_{k,2}\sin(\phi_{k2}+\phi_{s2})+\\ &\lambda\,\big(\Omega_1 x_{k+1,1}\sin(\phi_{k+1,1}+\phi_{s1})+\Omega_2 x_{k+1,2}\sin(\phi_{k+1,2}+\phi_{s1})\big)\Big)\Big],\end{aligned} \tag{A3}$$

$$\begin{aligned}\dot{\phi}_{k2} = -\frac{\epsilon}{\Omega_2 x_{k,2}}\,L_r\cos(\phi_{k2}+\phi_{s2})\Big[&R_2\Omega_2 x_{k,2}\sin(\phi_{k2}+\phi_{s2})+\\ &\Big(a-3\,b\,\big(x_{k,1}\cos(\phi_{k1}+\phi_{s1})+x_{k,2}\cos(\phi_{k2}+\phi_{s2})-\lambda\,\big(x_{k+1,1}\cos(\phi_{k+1,1}+\phi_{s1})+\\ &x_{k+1,2}\cos(\phi_{k+1,2}+\phi_{s2})\big)\big)^2\Big)\Big(-\Omega_1 x_{k,1}\sin(\phi_{k1}+\phi_{s1})-\Omega_2 x_{k,2}\sin(\phi_{k2}+\phi_{s2})+\\ &\lambda\,\big(\Omega_1 x_{k+1,1}\sin(\phi_{k+1,1}+\phi_{s1})+\Omega_2 x_{k+1,2}\sin(\phi_{k+1,2}+\phi_{s1})\big)\Big)\Big].\end{aligned} \tag{A4}$$

Appendix B: Averaged Equations for Bidirectional Coupling

$$\dot{x}_{k,1} = -\frac{\varepsilon}{\Omega_1}\sin\left(\phi_{k,1}+\phi_{s,1}\right)\Big[R_1 x_{k,1}\Omega_1\sin\left(\phi_{k,1}+\phi_{s,1}\right)+$$
$$\Big(a-3\,b\left(x_{k,1}\cos\left(\phi_{k,1}+\phi_{s,1}\right)+x_{k,2}\cos\left(\phi_{k,2}+\phi_{s,2}\right)-\lambda\left(x_{k+1,1}\cos\left(\phi_{k+1,1}+\phi_{s,1}\right)\right.\right.+$$
$$\left.\left.x_{k+1,2}\cos\left(\phi_{k+1,2}+\phi_{s,2}\right)+x_{k-1,1}\cos\left(\phi_{k-1,1}+\phi_{s,1}\right)+x_{k-1,2}\cos\left(\phi_{k-1}+\phi_{s,2}\right)\right)\right)^2\Big)$$
$$\Big(-\Omega_1 x_{k,1}\sin\left(\phi_{k,1}+\phi_{s,1}\right)-\Omega_2 x_{k,2}\sin\left(\phi_{k,2}+\phi_{s,2}\right)+\lambda\left(\Omega_1 x_{k+1,1}\sin\left(\phi_{k+1,1}+\phi_{s,1}\right)\right.$$
$$\left.+\Omega_2 x_{k+1,2}\sin\left(\phi_{k+1,2}+\phi_{s,2}\right)+\Omega_1 x_{k-1,1}\sin\left(\phi_{k-1,1}+\phi_{s,1}\right)+\right.$$
$$\left.\Omega_2 x_{k-1,2}\sin\left(\phi_{k-1}+\phi_{s,2}\right)\right)\Big)\Big], \tag{B1}$$

$$\dot{x}_{k,2} = -\frac{\varepsilon\, L_r}{\Omega_2}\sin\left(\phi_{k,2}+\phi_{s,2}\right)\Big[R_2\Omega_2 x_{k,2}\sin\left(\phi_{k,2}+\phi_{s,2}\right)+$$
$$\Big(a-3\,b\left(x_{k,1}\cos\left(\phi_{k,1}+\phi_{s,1}\right)+x_{k,2}\cos\left(\phi_{k,2}+\phi_{s,2}\right)-\lambda\left(x_{k+1,1}\cos\left(\phi_{k+1,1}+\phi_{s,1}\right)\right.\right.+$$
$$\left.\left.x_{k+1,2}\cos\left(\phi_{k+1,2}+\phi_{s,2}\right)+x_{k-1,1}\cos\left(\phi_{k-1,1}+\ \phi_{s,1}\right)+x_{k-1,2}\cos\left(\phi_{k-1}+\phi_{s,2}\right)\right)\right)^2\Big)$$
$$\Big(-\Omega_1 x_{k,1}\sin\left(\phi_{k,1}+\phi_{s,1}\right)-\Omega_2 x_{k,2}\sin\left(\phi_{k,2}+\phi_{s,2}\right)+\lambda\left(\Omega_1 x_{k+1,1}\sin\left(\phi_{k+1,1}+\phi_{s,1}\right)\right.$$
$$\left.+\Omega_2 x_{k+1,2}\sin\left(\phi_{k+1,2}+\phi_{s,2}\right)+\Omega_1 x_{k-1,1}\sin\left(\phi_{k-1,1}+\phi_{s,1}\right)+\right.$$
$$\left.\Omega_2 x_{k-1,2}\sin\left(\phi_{k-1}+\phi_{s,2}\right)\right)\Big)\Big], \tag{B2}$$

$$\dot{\phi}_{k1} = -\frac{\varepsilon}{\Omega_1 x_{k,1}}\cos(\phi_{k1}+\phi_{s1})\Big[R_1 x_{k,1}\sin(\phi_{k1}+\phi_{s1})+$$
$$\Big(a-3\,b\big(x_{k,1}\cos(\phi_{k1}+\phi_{s1})+x_{k,2}\cos(\phi_{k2}+\phi_{s2})-\lambda\left(x_{k+1,1}\cos(\phi_{k+1,1}+\phi_{s1})+\right.$$
$$\left.x_{k+1,2}\cos(\phi_{k+1,2}+\phi_{s2})+x_{k-1,1}\cos(\phi_{k-1,1}+\phi_{s1})+x_{k-1,2}\cos(\phi_{k-1,2}+\phi_{s2})\right)\big)^2\Big)$$
$$\Big(-\Omega_1 x_{k,1}\sin(\phi_{k1}+\phi_{s1})-\Omega_2 x_{k,2}\sin(\phi_{k2}+\phi_{s2})+\lambda\left(\Omega_1 x_{k+1,1}\sin(\phi_{k+1,1}+\phi_{s1})+\right.$$
$$\left.\Omega_2 x_{k+1,2}\sin(\phi_{k+1,2}+\phi_{s2})+\Omega_1 x_{k-1,1}\sin(\phi_{k-1,1}+\phi_{s1})+\Omega_2 x_{k-1,2}\sin(\phi_{k-1,2}+\phi_{s2})\right)\Big)\Big], \tag{B3}$$

$$\dot{\phi}_{k2} = -\frac{\varepsilon}{\Omega_2 x_{k,2}}\cos(\phi_{k2}+\phi_{s2})\Big[R_2\Omega_2 x_{k,2}\sin(\phi_{k2}+\phi_{s2})+$$
$$\Big(a-3\,b\big(x_{k,1}\cos(\phi_{k1}+\phi_{s1})+x_{k,2}\cos(\phi_{k2}+\phi_{s2})-\lambda\left(x_{k+1,1}\cos(\phi_{k+1,1}+\phi_{s1})+\right.$$
$$\left.x_{k+1,2}\cos(\phi_{k+1,2}+\phi_{s2})+x_{k-1,1}\cos(\phi_{k-1,1}+\phi_{s1})+x_{k-1,2}\cos(\phi_{k-1,2}+\phi_{s2})\right)\big)^2\Big)$$
$$\Big(-\Omega_1 x_{k,1}\sin(\phi_{k1}+\phi_{s1})-\Omega_2 x_{k,2}\sin(\phi_{k2}+\phi_{s2})+\lambda\left(\Omega_1 x_{k+1,1}\sin(\phi_{k+1,1}+\phi_{s1})+\right.$$
$$\left.\Omega_2 x_{k+1,2}\sin(\phi_{k+1,2}+\phi_{s2})+\Omega_1 x_{k-1,1}\sin(\phi_{k-1,1}+\phi_{s1})+\Omega_2 x_{k-1,2}\sin(\phi_{k-1,2}+\phi_{s2})\right)\Big)\Big]. \tag{B4}$$

* Electronic address: Pietro-Luciano.Buono@uoit.ca
† Electronic address: visarath@spawar.navy.mil; Electronic address: patrick.longhini@navy.mil
‡ Electronic address: loniolender@gmail.com; Electronic address: apalacios@mail.sdsu.edu
§ Electronic address: sireeves@ucsc.edu

[1] D. Allan, Tech. Rep. 1289, Hewlett Packard (1997).
[2] P.-L. Buono, B. Chan, J. Ferreira, A. Palacios, S. Reeves, V. In, and P. Longhini, SIAM J. Appl. Dynamical Systems **17**, 1310 (2018).
[3] J. Norie, New and Complete Epitome of Practical Navigation (1816).
[4] D. Lindley, *National science foundation: Coping with unusual atomic collisions makes an atomic clock more accurate*.
[5] D. Auston, Tech. Rep., National Research Council of the

National Academies, The National Academic Press, Washington D.C. (2002).
[6] NIST, *Nist launches a new u.s. time standard: Nist f2 atomic clock*.
[7] T. Heavner, E. Donley, F. Levi, G. Costanzo, T. Parker, J. Shirley, N. Ashby, S. Barlow, and S. Jefferts, Metrologia **51**, 174 (2014).
[8] M. Warren, Bell System Technical Journal **27**, 510 (1948).
[9] J. Semmlow, *Circuits, signals, and systems for bioengineers* (Academic Press, 2005).
[10] S. Voldman, *ESD: Failure Mechanisms and Models* (John Wiley and Sons, 2009).
[11] J. Laurin, S. Zaky, and K. Balmain, IEEE Transactions on Electromagnetic Compatibility **33**, 334 (1991).
[12] J. A. Sanders, F. Verhulst, and J. Murdock, *Averaging Methods in Nonlinear Dynamical Systems* (Springer, 2007), 2nd ed.
[13] M. Golubitsky, I. N. Stewart, and D. G. Schaeffer, *Singularities and Groups in Bifurcation Theory Vol. II*, vol. 69 (Springer-Verlag, New York, 1988).
[14] S. Wiggins, *Introduction to Applied Nonlinear Dynamical Systems* (Springer-Verlag, New York, 1990).
[15] V. In, A. Palacios, A. Bulsara, P. Longhini, A. Kho, J. Neff, S. Baglio, and B. Ando, Physical Review E **73**, 066121 (2006).
[16] G. Sebald, H. Kuwano, D. Guyomar, and B. Ducharne, Smart Materials and Structures **20**, 075022 (2011).
[17] E. Appleton and B. van der Pol, The London, Edinburgh, and Dublin Philosophical Magazine and Journal of Science Ser. 6 **43**, 177 (1922).
[18] B. V. der Pol, The London, Edinburgh, and Dublin Philosophical Magazine and Journal of Science Ser.7 **7**, 978 (1926).
[19] P. Holmes and D. Rand, Quart. Appl. Math. **35**, 495 (1978).
[20] B. van der Pol, The London, Edinburgh, and Dublin Philosophical Magazine and Journal of Science Ser. 7 **3**, 65 (1927).
[21] B. van der Pol and J. van der Mark, Nature **120**, 363 (1927).
[22] V. Apostolyuk and F. Tay, Sensor Lett. **2**, 252 (2004).
[23] N. Davies, Master's thesis, San Diego State University (2011).
[24] A. Shkel, in *Proceedings of IEEE/ION PLANS* (San Diego, CA, 2006), pp. 586–593.
[25] H. Vu, A. Palacios, V. In, P. Longhini, and J. Neff, Physical Rev. E. **81**, 031108 (2010).
[26] H. Vu, Ph.D. thesis, San Diego State University (2011).
[27] S. Beeby, M. Tudor, and N. White, Measurement Science and Technology **17**, R175 (2006).
[28] B.P.Mann and N.D.Sims, J. Sound and Vib. **319**, 515 (2009).
[29] C. Gardiner, *Handbook of Stachastic Methods 3rd Ed.* (Springer: Complexity, 2003).
[30] M. L. S. Wio, R. Deza, *An Introduction to Stochastic Processes and Nonequilibrium Statistical Physics* (World Scientific Publishing, 2012).
[31] B. Hajek, *An Exploration of Random Processes for Engineers* (2006).
[32] G. Adomian, **169** (1983).
[33] G. N. Mil'shtejn, Theory of Probability and Its Applications **19**, 557 (1975).
[34] W.J.Riley, Tech. Rep., Hamilton Technical Services, Beaufort, SC, USA, 29907 (2012).
[35] B. Montgomery, Cotts Journal Online (2005).